Broadband microwave absorption of sandwich-like RGA/CNP/RGA composites depending on strong polarization relaxations of multiscale interfaces

Mingtao Qiao[1,2]*, Jingyao Bai[1], Jiaoe Dang[3], Xingfeng Lei[2,4], Jiaxin Li[1], Jingbo Qi[1], Jian Wei[1], Qiuyu Zhang[2,4]

[1]College of Materials Science and Engineering, Xi'an University of Architecture & Technology, Xi'an 710055, Shaanxi, PR China

[2]School of Chemistry and Chemical Engineering, Northwestern Polytechnical University, Xi'an 710072, PR China

[3]Instrumental Analysis Center, Xi'an University of Architecture and Technology, Xi'an 710055, Shaanxi, PR China

[4]MOE Key Laboratory of Material Physics and Chemistry under Extraordinary Condition, Ministry of Education, Northwestern Polytechnical University, Xi'an 710072, PR China

Characterizations

Scanning electron microscopy (SEM, GeminiSEM500) transmission electron microscope (TEM, Talos F200X) were performed to observe the microstructure and morphology of the samples. X-ray diffraction patterns (XRD) were obtained via the Shimadzu XRD-7000s diffractometer with Cu Kα radiation (λ = 1.542 Å) from 20° to 80°. Raman spectroscopy of the samples was obtained by a Renishaw in Via Raman Microscope. The N_2 adsorption/desorption isotherms were recorded on a TriStar II 20 apparatus, and the specific surface area and pore volume analysis were performed by Brunauer-Emmett-Teller (BET) and Barrett-Joyner-Halenda (BJH) methods, respectively. The chemical binding of the samples was detected by X-ray photoelectron spectroscopy (XPS, Thermo Scientific). The magnetic properties of products were assessed using a vibrating sample magnetometer (VSM, LakeShore 7307) at room temperature. Electromagnetic parameters were measured by vector network analyses (VNA, Agilent, N5227, USA) equipped with a coaxial transmission waveguide in the frequency range 2-18 GHz.

Figure S1. the schematic illustration of multilayered RGA/CNP composites, (S1) Janus RGA/CNP, (S2) three-layer RGA/CNP, (S3) five-layer RGA/CNP, (S4) seven-layer RGA/CNP composites.

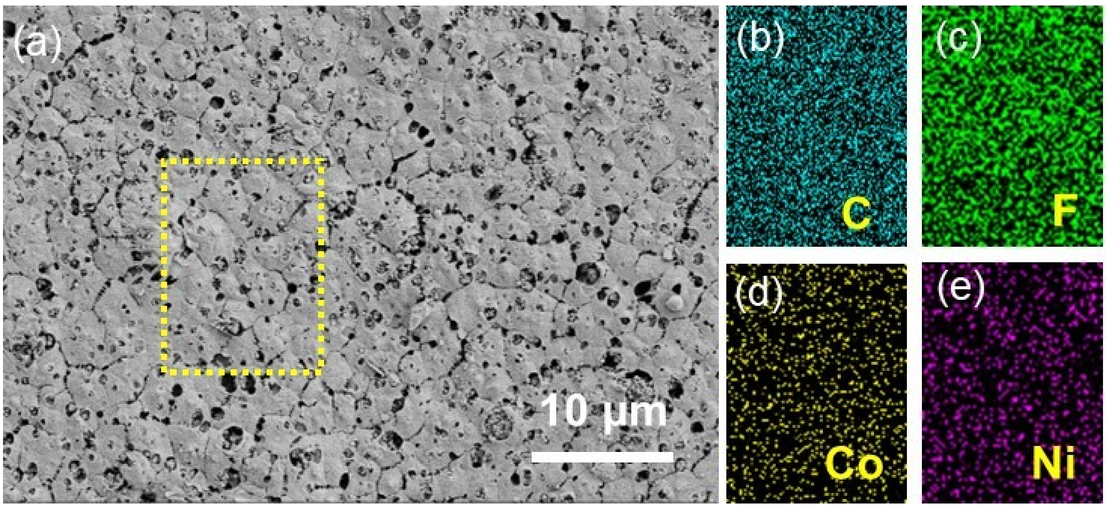

Figure S2. (a) SEM image and (b-e) EDS images of CNP films

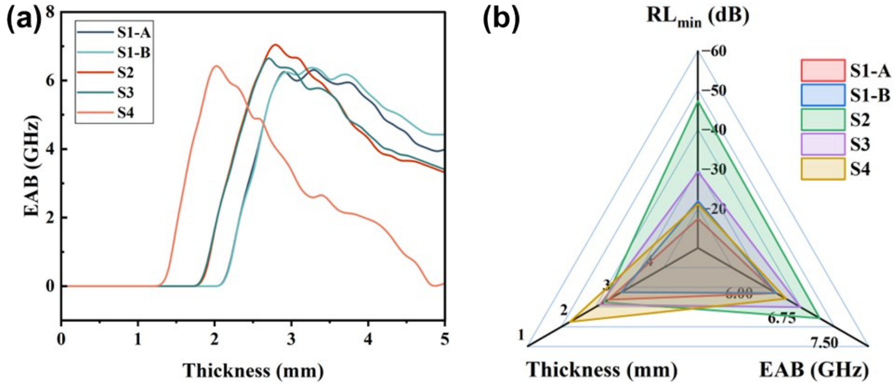

Figure S3. (a) The trend curves of EAB with increasing the layer thickness, and (b) the corresponding radar map.

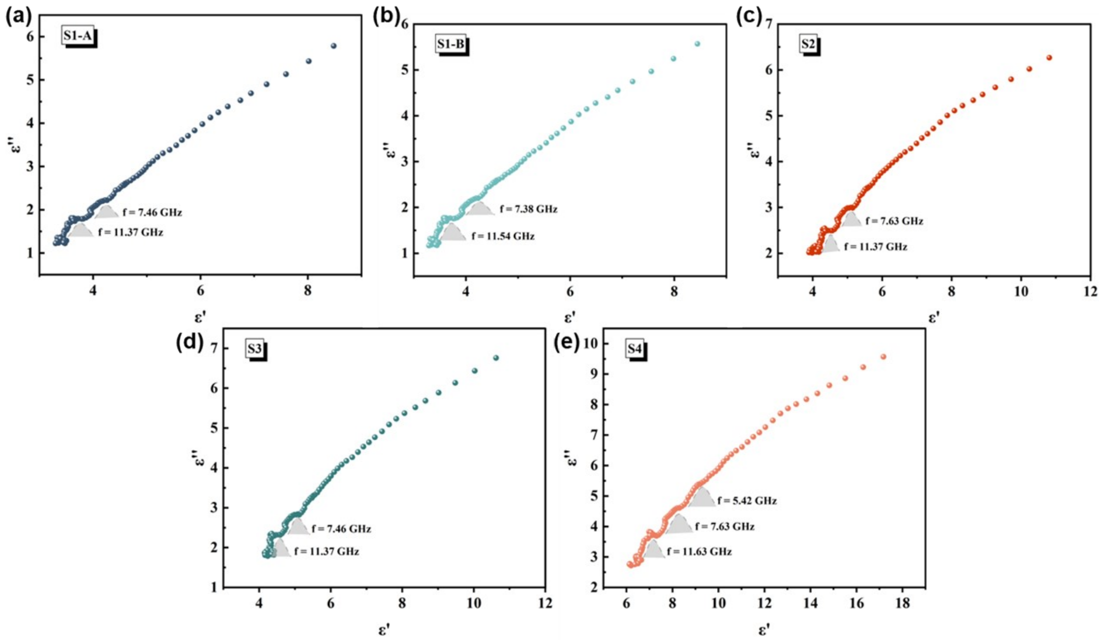

Figure S4. The Cole-Cole curves of samples

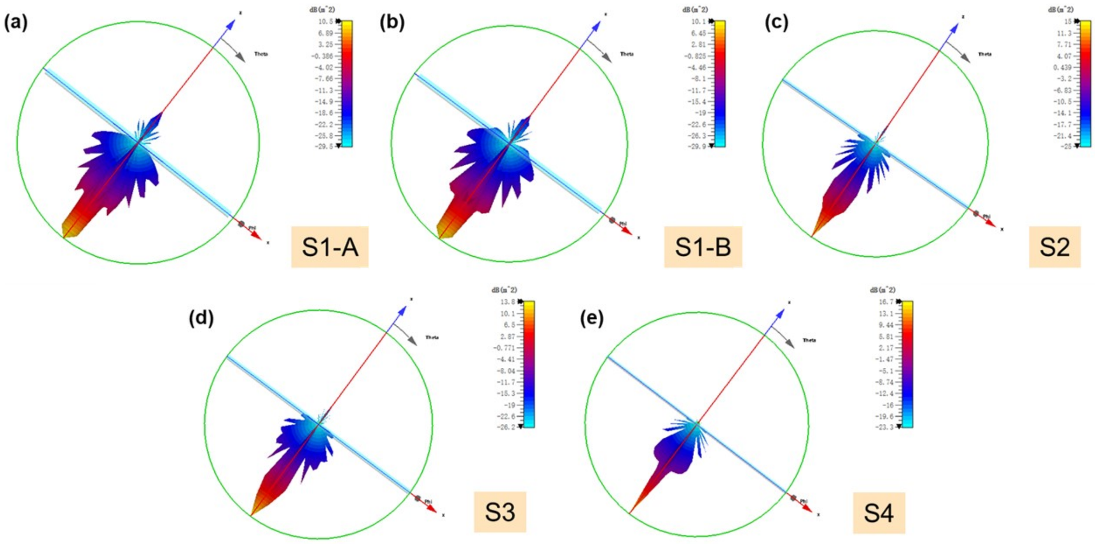

Figure S5. 3D CST far-field simulation results for samples

Table S1. The comparison among similar microwave absorbers

Samples	RL_{min}(dB)/ Thickness(mm)	EAB_{max}(GHz)/ Thickness(mm)	Refs
Co/C	−38.8/1.82	4.7/1.5	[1]
Ni/C	−26.3/2.3	5.2/1.8	[2]
CoNi@C	-47.1/2.0	5.1/1.7	[3]
CoNi@C@rGO	-48/4.5	6.24/1.6	[4]
Co_2Ni_1/C-800/PVDF	-52/3.0	4.5/3.0	[5]
Ni@C-rGO	-53.64/4.1	6.64/2.55	[6]
CoNi-C aerogels	-40.69/2.41	5.7 /1.76	[7]
Co@RGA microspheres	-70.4/2.2	5.65/1.98	[8]
2D CoNi/C	-60.1/1.65	6.24/1.0	[9]
CoNi@carbon/RGO	-41.09/1.5	5.41/1.5	[10]
Ni-MOF-rGO aerogel	-51.19/1.9	6.32/1.9	[11]
CoNi/carbon foam	-47.35/2.4	5.6/2.4	[12]
MXene-CNTs/Co	-41.29/1.38	4.2/1.38	[13]
CoNi/C	−61.02/2.0	5.2/2.0	[14]
RGA/CNP/RGA	-48.03/2.7	7.14/2.8	Herein

Table S2. The order of samples in the microwave absorption properties

Microwave absorption properties	The order of samples
Effective absorption bandwidth	S2>S3>S4
Impedance matching ($\lvert Z_{in}/Z_0\rvert$)	S2≈S3>S4
Conductive loss	S4>S3>S2>S1
Polarization loss	S4>S2>S3>S1
Dielectric loss tangent (tan δ_ε)	S4>S2≈S3>S1 (tan δ_ε > 0.4)
Magnetic loss tangent (tan δ_μ)	S4>S2≈S3≈S1 (tan δ_μ < 0.4)
Attenuation coefficient (α)	S4>S2>S3>S1

The related theory equations:

(1) According to the transmission line theory in the metallic backing condition, the calculation formula of the RL-*f* curves are as follows [15,16]:

$$\mathrm{RL} = 20\lg_{10}\left|(Z_{in}-Z_0)/(Z_{in}+Z_0)\right| \quad (1)$$

$$\mathrm{Z_{in}} = \mathrm{Z_0}\sqrt{\frac{\mu_r}{\varepsilon_r}}\tanh\left(j\frac{2\pi fd\sqrt{\mu_r\varepsilon_r}}{c}\right) \quad (2)$$

Where Z_0 is the characteristic impedance of free space, Z_{in} is the normalized input impedance of absorber, ε_r and μ_r are the relative complex permittivity and permeability, d is the layer thickness, c is the speed of light in free space and f is the frequency.

(2) According to the Debye theory, Cole–Cole semicircle model can be expressed by the following equations [15, 17]:

$$\varepsilon' = \frac{\varepsilon_s-\varepsilon_\infty}{1+\omega^2\tau^2}+\varepsilon_\infty \quad (3)$$

$$\varepsilon'' = \varepsilon_p'' + \varepsilon_c'' = \omega\tau\frac{\varepsilon_s-\varepsilon_\infty}{1+\omega^2\tau^2}+\frac{\sigma}{\varepsilon_0\omega} \quad (4)$$

$$\left(\varepsilon' - \frac{\varepsilon_s+\varepsilon_\infty}{2}\right)^2 + (\varepsilon'')^2 = \left(\frac{\varepsilon_s-\varepsilon_\infty}{2}\right)^2 \quad (5)$$

where τ represents relaxation time, ε_s and ε_∞ represent static permittivity and optical permittivity respectively.

(3) The eddy current loss C_0 of magnetic loss materials is expressed by the following equation [16, 18]:

$$C_0 = \mu''(\mu')^{-2} f^{-1} = 2\pi\mu_0\sigma d^2 / 3 \tag{6}$$

(4) The attenuation ability of the materials can be assessed by attenuation coefficient (α) as followed [15, 19]:

$$a = \frac{\sqrt{2}\pi f}{c} \times \sqrt{(\mu''\varepsilon'' - \mu'\varepsilon') + \sqrt{(\mu''\varepsilon'' - \mu'\varepsilon')^2 + (\mu'\varepsilon'' + \mu''\varepsilon')^2}} \tag{7}$$

(5) The percentage of dielectric loss and magnetic loss can be expressed by the following equations:

$$W_c = \frac{\varepsilon_c''}{\varepsilon'' + \mu''} \tag{8}$$

$$W_p = \frac{\varepsilon_p''}{\varepsilon'' + \mu''} \tag{9}$$

$$W_m = \frac{\mu''}{\varepsilon'' + \mu''} \tag{10}$$

where W_c, W_p, W_m represents the percentage of conductive loss, polarization loss and magnetic loss in the attenuation process respectively.

(6) The RCS values can be calculated as follows [20, 21]:

$$\sigma(dBm^2) = 10\log\left[\frac{4\pi S}{\lambda^2}\left|\frac{E_s}{E_i}\right|^2\right] \tag{11}$$

Where E_i and E_s represent the electric field strength of the incident and scattered waves, respectively, S is area of the simulated plate and λ is the wavelength.

References

[1] Xie P, Liu Y, Feng M, et al. Hierarchically porous Co/C nanocomposites for ultralight high-performance microwave absorption. Advanced Composites and Hybrid Materials, 2021, 4: 173-185.

[2] Zhang Y, Zhang X, Quan B, et al. A facile self-template strategy for synthesizing 1D porous Ni@ C nanorods towards efficient microwave absorption. Nanotechnology, 2017, 28(11): 115704.

[3] Shen Z, Yang H, Xiong Z, et al. Hollow core-shell CoNi@C and CoNi@NC composites as high-performance microwave absorbers. Journal of Alloys and Compounds, 2021, 871: 159574.

[4] Peng K, Wu Y, Fang G, et al. Self-assembly hollow magnetoelectric composites emerging tunable property between microwave absorption and shielding with light-weight and broad bandwidth. Journal of Alloys and Compounds, 2023, 947: 169368.

[5] Wang Y L, Wang G S, Zhang X J, et al. Porous carbon polyhedrons coupled with bimetallic CoNi alloys for frequency selective wave absorption at ultralow filler loading. Journal of Materials Science & Technology, 2022, 103: 34-41.

[6] Qiu J, Liu X, Peng C, et al. Porous metal microsphere M@C-rGO (metal= Mn, Fe, Co, Ni, Cu) aerogels with high low-frequency microwave absorption, strong thermal insulation and superior anticorrosion performance. Journal of Materials Chemistry A, 2024, 12(33): 21997-22012.

[7] Xu Q, Zhu X, Yu J, et al. Constructing core-shell structural bimetallic CoNi alloys doped carbon aerogels for highly efficient electromagnetic wave absorption. Journal of Alloys and Compounds, 2025: 178854.

[8] Xu Q, Zhu X, Yu J, et al. Constructing core-shell structural bimetallic CoNi alloys doped carbon aerogels for highly efficient electromagnetic wave absorption. Journal of Alloys and Compounds, 2025: 178854.

[9] Huang W, Song M, Wang S, et al. Dual-step Redox Engineering of Two-Dimensional CoNi-Alloy Embedded B, N-Doped Carbon Layers towards Tunable Electromagnetic Wave Absorption and Light-Weight Infrared Stealth Heat Insulation Devices. Advanced Materials, 2024: 2403322.

[10] Ma C, Zhang C, Yuan M, et al. ZIF-67 derived CoNi@carbon/RGO composites with abundant heterogeneous interfaces for electromagnetic wave absorption. Applied Surface Science, 2024, 665: 160283.

[11] Cao K, Yang X, Zhao R, et al. Fabrication of an ultralight Ni-MOF-rGO aerogel with both dielectric and magnetic performances for enhanced microwave absorption: microspheres with hollow structure grow onto the GO nanosheets. ACS Applied Materials & Interfaces, 2023, 15(7): 9685-9696.

[12] Guo X, Nie Z, Feng Y, et al. In situ growth of CoNi alloy/N-doped hollow carbon foam for electromagnetic wave absorption. ACS Applied Nano Materials, 2024, 7(16): 19427-19438.

[13] Yongqi Zhao, Jingjing Wang, Danyi Yang, et al. MXene-CNTs/Co dielectric-electromagnetic synergistic composites with multi-heterogeneous interfaces for microwave absorption [J]. Carbon, 2025, 232: 119825.

[14] Kai Lin, Lingyun Wu, Tianyu Wu, et al. Bimetal-doped core-shell carbon derived from

nickel-cobalt dual-ligand metal-organic framework for adjustable strong microwave absorption [J]. Journal of Colloid and Interface Science, 2022, 627: 90-101.
[15] Song L, Wu C, Zhi Q, et al. Multifunctional SiC aerogel reinforced with nanofibers and nanowires for high-efficiency electromagnetic wave absorption. Chemical Engineering Journal, 2023, 467: 143518.
[16] Li K, Han L, Wang T, et al. 4D printing MOF-derived/multi-fluorination nanocomposites for ultra-efficient electromagnetic wave absorption and robust environment adaptivity. Journal of Materials Chemistry A, 2024, 12(11): 6302-6317.
[17] He Z, Xu H, Shi L, et al. Hierarchical Co_2P/CoS_2@C@MoS_2 composites with hollow cavity and multiple phases toward wideband electromagnetic wave absorption. Small, 2024, 20(6): 2306253.
[18] Chen Y, He W, Zhou H, et al. Compressible and conductive multi-scale composite aerogel elastomers for electromagnetic wave absorption, energy harvesting, and piezoresistive sensing. Nano Energy, 2024, 119: 109100.
[19] Feng S, Wang H, Ma J, et al. Fabrication of hollow Ni/NiO/C/MnO_2@ polypyrrole core-shell structures for high-performance electromagnetic wave absorption. Composites Part B: Engineering, 2024, 275: 111344.
[20] Huang M, Wang L, Pei K, et al. Heterogeneous Interface Engineering of Bi-Metal MOFs-derived $ZnFe_2O_4$-ZnO-Fe@C Microspheres via Confined Growth Strategy Toward Superior Electromagnetic Wave Absorption. Advanced Functional Materials, 2024, 34(3): 2308898.
[21] Rao L, Wang L, Yang C, et al. Confined diffusion strategy for customizing magnetic coupling spaces to enhance low-frequency electromagnetic wave absorption. Advanced Functional Materials, 2023, 33(16): 2213258.